Materials Science & Engineering A 824 (2021) 141857

Contents lists available at ScienceDirect

Materials Science & Engineering A

journal homepage: www.elsevier.com/locate/msea

Effect of equal-channel angular pressing on microstructural evolution, mechanical property and biodegradability of an ultrafine-grained zinc alloy

Xiuping Wang [a], Yan Ma [b], Bao Meng [a,*], Min Wan [a]

[a] School of Mechanical Engineering and Automation, Beihang University, Beijing, 100191, PR China
[b] Department of Microstructure Physics and Alloy Design, Max-Planck-Institut für Eisenforschung GmbH (MPIE), Max-Planck-Str. 1, 40237, Düsseldorf, Germany

ARTICLE INFO

Keywords:
Zinc alloy
Equal-channel angular pressing (ECAP)
Discontinuous yielding
Microstructural evolution
Mechanical properties
Corrosion behavior

ABSTRACT

Zinc alloys have become one of the most promising material groups for biodegradable medical implants due to their desirable degradability, excellent biocompatibility, unique atherosclerotic resistance, and modest mechanical performance. Grain refinement is an important strengthening mechanism for such an alloy system to improve the mechanical properties. In the present work, an ultrafine-grained (UFG) zinc alloy (Zn-0.033 Mg, in wt.%) was fabricated by equal-channel angular pressing (ECAP) process. The effect of the ECAP process on microstructural evolution, mechanical properties, and biodegradability of the material was investigated. The results indicated that a large number of sub-boundary and recrystallized-grain structures were generated by continuous and discontinuous dynamic recrystallization during severe plastic deformation. Grain size was significantly refined to an average grain size of 1.36 ± 0.90 μm, and the percentage of grains below 1 μm reached 37.4% after 12 ECAP passes. Simultaneously, the texture was changed from the extrusion direction (ED)‖<0001> fiber texture to a texture with ED deviating 70 ± 5° away from <0001>. Due to the synergy effect of grain refinement and texture, as well as dislocation strengthening, the yield strength was enhanced to 276 ± 3 MPa after 12 ECAP passes. However, this was inevitably accompanied by a sacrifice of elongation (8.17 ± 1.21%). Therefore, an optimal combination of yield strength (250 ± 22 MPa) and elongation (25.37 ± 0.79%) at room temperature was obtained after 4 ECAP passes. Moreover, a low corrosion rate of 0.004–0.01 mm/year in the UFG Zn-0.033 Mg alloy fabricated by ECAP was achieved, which fully satisfies the requirements for biodegradable implant materials.

1. Introduction

Zinc-magnesium (Zn–Mg) alloys are increasingly used as next-generation biodegradable implant materials due to their superior mechanical properties, appropriate degradation rates in vivo, and desirable biocompatibility [1,2]. Compared with traditional biodegradable biomaterials such as polymers, ceramics, as well as magnesium alloys and iron alloys, Zn–Mg alloys exhibit superior strength compared to low strength polymers, and have improved corrosion rates compared to magnesium alloys and iron alloys, which are either too fast or too slow [3,4]. Furthermore, zinc is an indispensable element for cell growth and wound healing, and the degradation products of zinc contribute to the anti-proliferation and prevention of restenosis during the treatment [5]. Unfortunately, cast Zn–Mg alloys have insufficient mechanical properties for stent applications [6].

Equal-channel angular pressing (ECAP) is one of the most promising techniques to refine materials' microstructure via severe plastic deformation and prepare large bulk metal materials with enhanced yield strengths. Tong et al. [7] successfully prepared the Mg–Zn–Ca–Mn alloy with an average grain size of ~1 μm through ECAP with high yield strength (~261.4 MPa) and superior ductility (~19.29%) properties compared to the traditional hot-extruded one, which had a yield strength of only 229 MPa and elongation to fracture of 10% [8]. The researchers stated that the combination of strength and ductility was attributed to homogenous deformation as a result of the ECAP process, which promoted prominent grain refinement and the coordination of non-basal slip systems. Yan et al. [9] also reported the effects of ECAP on the microstructure of Mg–6Zn alloy, and decreased the grain size from ~15 μm to 1–4 μm after 6 ECAP passes at 433 K. The effective refinement mechanism was characterized as the synergistic effect of dynamic recrystallization (DRX) and the pinning effect of the fine particles. Ma et al. [10] also prepared a fine-grained Mg alloy through a two-step

* Corresponding author.
E-mail address: mengbao@buaa.edu.cn (B. Meng).

https://doi.org/10.1016/j.msea.2021.141857
Received 12 April 2021; Received in revised form 28 July 2021; Accepted 31 July 2021
Available online 1 August 2021

low-temperature ECAP method. They found that low-temperature ECAP deformation could only refine the size of the second phase particles, but no changes were observed in their distribution, which would restrict DRXed grains growth with the pinning effect. In addition, Wang et al. [11] comparatively studied the as-cast and as-homogenized states of Mg alloys after 2 ECAP passes, and found that the second phase particles effectively promoted the microstructural refinement and mechanical improvements. Skryabina et al. [12] investigated the effects of ECAP temperature, and the number of the ECAP passes on the microstructure transformation of AZ31. They suggested that it was helpful to produce an ultrafine-grained structure when the temperature was kept low enough to inhibit the fast recrystallization process. Tong et al. [13] also achieved significant grain refinement of an equal-channel angular pressed (ECAPed) Mg alloy with an average grain size of ~0.9 μm, and the improvement in both yield strength and elongation. Furthermore, they concluded that the grain refinement mechanism was related to the low-temperature progressive recrystallization process.

The influence of the ECAP process on mechanical properties can be categorized into two aspects: boundary strengthening and texture modification effect. The latter depends on the specific alloy and processing conditions. For example, Suresh et al. [14] performed 4 ECAP passes on AA2195 and achieved a significant refinement, with a smaller average grain size of 2.8 μm compared to the initial grain size of 56 μm. They observed that the slip activities per grain became more and more active during ECAP, but the texture after ECAP overall weakened. Martynenko et al. [15] also analyzed the effect of texture evolution on mechanical properties during ECAP by assessing an Mg–Zn–Ca alloy after 10 ECAP passes. They suggested that during the ECAP process the alloy exhibited weakened texture effect due to the dispersed orientations. The deformed texture caused a decrease in strength and tensile-compression asymmetry, and was accompanied by the prismatic slip, which was the predominant deformation mode without changes in the activity of the pyramidal slip and twinning. Wang et al. [16] compared the microstructural evolution of the cold-drawn Zn-0.02 Mg and cold-drawn AZ31 wires, and found that the former had an increasing intensity texture with deviating from the <0001> and the latter exhibited a decline in basal fiber texture intensity. They surmised that the two alloys, zinc and magnesium, both had hexagonal close-packed (HCP) crystal structure, and exhibited significant differences in the evolution of microstructure, texture, and deformation mechanism during drawing. The effects of ECAP on grain refinement and mechanical properties of Zn-0.8Ag, Zn-0.5Cu and Zn-0.4Mn alloys at room temperature were also investigated by Bednarczyk et al. [17]. The authors observed that the effects of various alloying elements in zinc alloys during ECAP treatment differed, in terms of their microstructural evolution and mechanical properties, and their deformation mechanisms during tensile testing.

Previous studies have demonstrated that ECAP is a powerful manufacturing technique for improving the mechanical properties of metallic materials, by grain boundary strengthening, second phase particle strengthening, and texture modification via grain refinement. This makes it attractive to apply such a manufacturing technique also for zinc alloys, to improve their mechanical performances. For HCP metals, the c/a ratio is a critical parameter for the mode of plastic deformation, where a denotes the hexagonal dimensions, and c denotes the elementary cell extension along the hexagonal axis [18]. Unlike most HCP metals, the c/a ratio of zinc is 1.853, which exceeds 1.633 (the ideal c/a ratio of HCP metals). Thus, the deformation mechanisms observed in zinc alloys during ECAP may significantly differ from other HCP metals, such as magnesium (c/a ratio of 1.623). In addition, the recrystallization temperature of zinc is supposed to be approximately 261 K [17], and that of zinc alloy is also low, and is very close to room temperature (293 K). It has been reported that during ECAP, when a large strain was applied, DRX could occur at a lower temperature [19]. Therefore, the comprehensive effects of the ECAP process on the microstructural evolution, macro-mechanical behavior, and service performance of zinc alloys with ultrafine grains are not fully understood. Furthermore, existing studies on Zn–Mg alloys are limited, including microstructure, mechanical property, corrosion property, biocompatibility assessments. These alloys have relatively high levels of Mg content. Previous research has suggested that an increase in Mg content enhances the strength of the material, but deteriorates the balance of ductility and strength [20], either or reduces corrosion resistance due to the increasing Mg_2Zn_{11} phase, which easily forms a galvanic cell with α-Zn matrix [21]. Thus, to satisfy the requirements for implants, a trace amount of 0.033% by weight of Mg was chosen to design the special Zn–Mg alloy, with a minimal secondary phase to avoid brittleness and pitting corrosion.

In this study, the ultrafine-grained zinc alloy was produced using a multi-pass ECAP process, and the microstructural evolution, mechanical properties, and corrosion behavior of the alloy after several ECAP passes were systematically investigated. Our findings provide new information regarding the performance of zinc alloys and provide new insights into the application of zinc alloys in degradable implants.

2. Experimental methods

2.1. Material and processing

In this study, a zinc alloy with a nominal chemical composition of Zn-0.033 Mg (in wt.%) was fabricated by smelting, casting, heat treatment, and extrusion. The fabrication processes are schematically illustrated in Fig. 1. Commercially pure zinc (99.95 wt%) and pure magnesium (99.95 wt%) ingots were melted in a well-type resistance furnace at a temperature of 843 K. Subsequently, the laboratory-processed alloy was cast at 773 K in a cylindrical steel mold with a diameter of 120 mm. Two-step homogenization treatment was then performed at 573 K for 2 h, then at 613 K for 2 h, followed by cooling in open air to room temperature. A two-step swaging process was then conducted to further reduce the rod diameter. Subsequently, the Zn-0.033 Mg rods were swaged at 623 K to a diameter of 50 mm, then transformed to a diameter of 46 mm, and finally extruded at 373 K to a diameter of 10 mm with a swaging speed of 1 mm/s. The swaged rods were further machined into

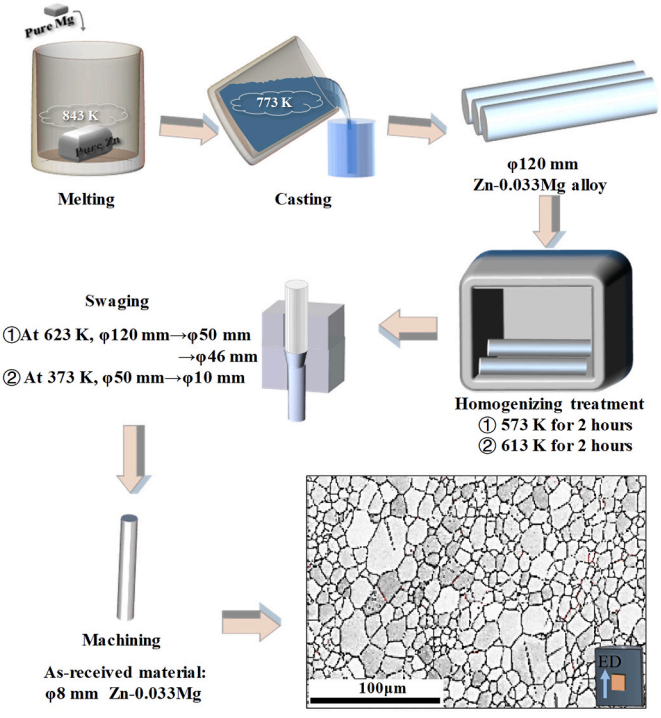

Fig. 1. Schematic illustration of the fabrication processes of the Zn-0.033 Mg (in wt.%) alloy.

cylindrical samples with a diameter of 8 mm and a length of 60 mm. These were denoted as the as-received samples.

2.2. Equal-channel angular pressing

Equal-channel angular pressing (ECAP) was further employed to manufacture the ultrafine-grained (UFG) Zn-0.033 Mg alloy. The ECAP setup, consisting of a heating device and an ECAP die, is shown in Fig. 2a. The latter part contained two equal diameter channels, with an inclined angle of 90°. The diameters of the vertical and horizontal channels were 10.1 and 9.9 mm, respectively. Such a difference in channel diameter was necessary to easily feed the workpieces in multiple passes. In addition, the radii of the inner and outer corners were 1.5 and 3.4 mm, respectively. Because the ECAP process can induce undesirable jagged cracks on the surface of a brittle material, 1 mm copper cladding was adopted on the surface of the as-received Zn-0.033 Mg rods, for protection. The ECAP process was conducted according to the route shown in Fig. 2b. During each pass, the sample was inverted and rotated 90° clockwise around the longitudinal axis. The first pass was conducted at room temperature. Owing to their HCP crystal structure, zinc alloys usually exhibit poor forming abilities at room temperature. Thus the warm ECAP at an elevated temperature of 416 K was utilized from the second pass to improve the formability of the Zn-0.033 Mg alloy. The die was preheated for half an hour before the second ECAP process to ensure homogeneous temperature distribution in the die. The molybdenum disulfide was utilized as a lubricant to reduce any adverse friction forces at the die/sample interface. Finally, prior to warm ECAP, the sample was preheated in the channel for 10 s, and then extruded at a speed of 6 mm/s. To reveal the effect of grain size on mechanical properties of the Zn-0.033 Mg alloy, the ECAP process with various passes, *i.e.,* 4, 8, and 12 passes, was performed to adjust grain size. The ECAPed samples (Fig. 2c) were denoted as 4p-, 8p-, and 12p-ECAPed samples according to the number of ECAP passes.

2.3. Microstructure characterization

The microstructures of the as-received and ECAPed materials were characterized using an Oxford scanning electron microscope equipped with electron backscatter diffraction (EBSD). The EBSD specimens were mechanically grounded using progressively fine grit sand papers, and then polished in the electrolytic mixtures of 7% $HClO_4$ and 93% C_2H_5OH, with the current density of 450 mA/cm^2 for 1 minute. The observations of the as-received and ECAPed materials were conducted on the radical plane and the longitudinal plane (perpendicular to extrusion direction (ED)), respectively. The corresponding specimens were taken from the center of the rods, as shown in Fig. 3. The step sizes for EBSD measurements were 1.1 and 0.08 μm for the as-received and ECAPed specimens, respectively. The acquired EBSD data were then

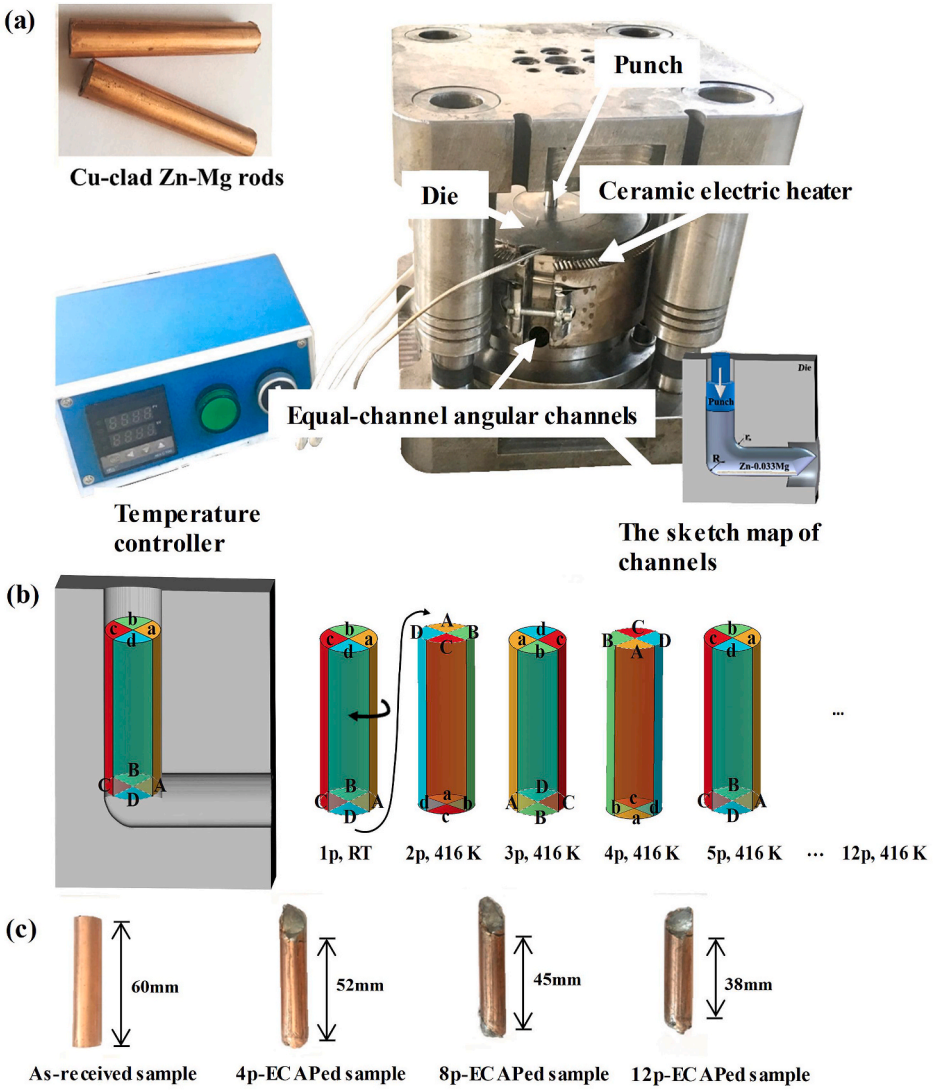

Fig. 2. The ECAP setup and process route: (a) ECAP die; (b) ECAP route and (c) ECAPed samples.

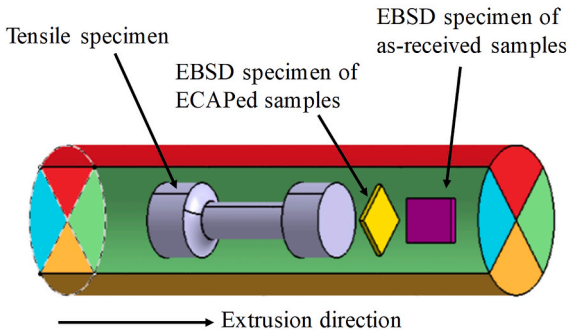

Fig. 3. Locations of the tensile and EBSD specimens in the as-received and ECAPed materials.

reconstructed using Channel 5 commercial software.

2.4. Mechanical testing

The mechanical properties were evaluated by uniaxial tensile tests, which were conducted on a tensile machine at room temperature. The initial strain rate was set to 10^{-3} s^{-1}. Dog-bone–shaped rod specimens were cut along the ED (as shown in Fig. 3), and the gauge length and diameter of the tensile specimens were 12.5 and 4 mm, respectively. The ECAPed-sample was whittled from ECAPed samples to a thickness of 2 mm in the radial direction, thereby the copper cladding was completely removed. In addition, reports have shown that this composite interface by diffusion in cladding metals, where the region was merely a few microns in thickness [22], was not readily to form or could be destroyed by huge shearing force during severe plastic deformation [23]. Therefore, the effect of the copper cladding material on the mechanical performance of Zn-0.033 Mg was negligible. A grating displacement sensor was also used to quantify the deformation strain. Three tests were repeated for each condition to ensure repeatability.

2.5. Corrosion tests

To assess the degradation behavior, the immersion tests were performed in Hank's solution, which consists of 8.00 g/L NaCl, 0.40 g/L KCl, 1.0 g/L glucose, 0.0358 g/L Na_2HPO_4 (anhydrous), 0.06 g/L KH_2PO_4, 0.072 g/L $CaCl_2$, 0.123 g/L $MgSO_4{\cdot}7H_2O$ and 0.35 g/L $NaHCO_3$. The specimens were cut from the rods stripped off copper cladding, and manufactured into disks. The diameter and thickness of disks were 6 mm and 2 mm, respectively. The specimens were grounded using SiC paper down to 2000 grit, cleaned with ethanol in an ultrasonic bath, and then dried in ambient air. The specimens were immersed in Hank's solution for 1, 2, 4, 8, and 14 days. The Hank's solution was kept at 310 ± 1 K and 7.4 pH during the tests and changed every 24 h. After immersion testing, the corrosion products were removed using a chromic acid solution (200 g/L CrO_3 + 10 g/L $AgNO_3$ + deionized water) in an ultrasonic bath. To calculate the weight loss, the specimens were weighed using an electronic balance with an accuracy of 0.0001 g, before and after immersion testing. The corrosion rate was further calculated according to the following formula:

$$V = K{\cdot}(W_1 - W_0)/(S \times t \times \rho) \quad (1)$$

Where K is the conversion coefficient for the corrosion rate of millimeters per year, W_1 and W_0 are the weights of the corroded specimen and initial one, S is the surface area of the specimen, t is the corrosion time in an hour, and ρ is the alloy density.

3. Results and discussion

3.1. Effects of ECAP on microstructural evolution

3.1.1. Microstructure of as-received material

Fig. 4 shows the microstructure of the as-received sample. A heterogeneous microstructure was characterized by the mixture of coarse and fine grains in bands along ED direction. According to grain size and orientation, the fine-grained bands were interspersed with coarse grains. It could be inferred in the material preparation stage, the coarse original grains became fragmented and split into deformation bands, which were energetically easier to deform in fewer than the five slip systems requiring for restricted deformation [24]. The grain bands were subsequently subdivided by the expansion and contraction of grain boundaries due to strain energy and combined with the newly-subdivided grains [14]. The inverse pole figure (IPF) of the full DRXed fine grains was mostly coded in red (Fig. 4a). This indicated a significantly preferred orientation for the DRXed grains, i.e. the <0001> direction parallel to ED. Furthermore, a small amount of stretched twins with a misorientation of 86.5° and DRXed grains of the "necklace" structure were observed in Fig. 4a. A typical fiber texture in the ED plane tended to rotate about 20 ± 5° away from the ED || <0001> existing a maximum pole intensity of 2.1, as displayed in the triangular IPF map in the ED (Fig. 4b) and the {0001} pole figure (Fig. 4c). Fig. 4d shows the grain boundary profile, with the high-angle grain boundaries (HAGBs, misorientations > 15°) and low-angle grain boundaries (LAGBs, misorientations between 2° and 15°), as highlighted by the black and the red lines, respectively. The misorientation angle distribution frequency between adjacent grain boundaries is plotted in Fig. 4f. The average misorientation θ_{av} was 50.6° and the HAGBs fraction was up to 94.8%, while the LAGBs were uniformly distributed. This indicated the deformation of as-received material was termed as continuous DRX due to the HAGBs fraction was an important parameter for the determination of continuous recrystallization [25]. The average grain size of the as-received material was 9.02 ± 4.37 μm, and numerous grains were in a size range of 3.5–11.5 μm (Fig. 4e). Moreover, there was a higher fraction peak near the misorientation of 86.5°, which was consistent with the deformation twin boundaries (as shown in Fig. 4a). This peak was possibly related to the high intensity of the fiber texture with {0001} plane inclined about 20° toward ED (in Fig. 4c) and the large grain size [26]. Combined with the boundary profile shown in Fig. 4d, grains with HAGBs dominated in the material, indicating a completely recrystallized state of the as-received material. Therefore, the microstructural evolution in this stage was dominated by deformation bands and continuous DRX.

Fig. 5 shows the Schmid factor distributions of the various major slip systems. The results showed a higher Schmid factor value of a basal slip and <c+a>-pyramidal slip systems. This indicated that most grains possessed soft orientations (with their basal planes and c-axis inclined toward the main slip plane), once the tensile stress was aligned with ED [7]. The pyramidal slip was subjected to actuate and coordinate deformation with the basal slide. Thus, plastic deformation of the as-received sample was dominated by the slip of the basal plane, complemented by <c+a>-pyramidal slip.

3.1.2. Microstructural evolution of ECAPed alloy

To fully understand microstructural evolution during ECAP and the underlying grain refinement mechanism caused by severe plastic deformation, the microstructural characteristics of specimens after various ECAP passes were analyzed and compared. The results showed that the microstructure of the Zn-0.033 Mg alloy was significantly refined by ECAP and did not show obvious preferred orientation (Fig. 6). The average grain sizes were 1.53 ± 0.81 μm, 1.71 ± 0.94 μm, and 1.36 ± 0.90 μm for 4p-, 8p- and 12p-ECAPed samples, respectively. Grain size inhomogeneity was significantly eliminated in the ECAPed samples compared to the as-received material. The fine grains completely

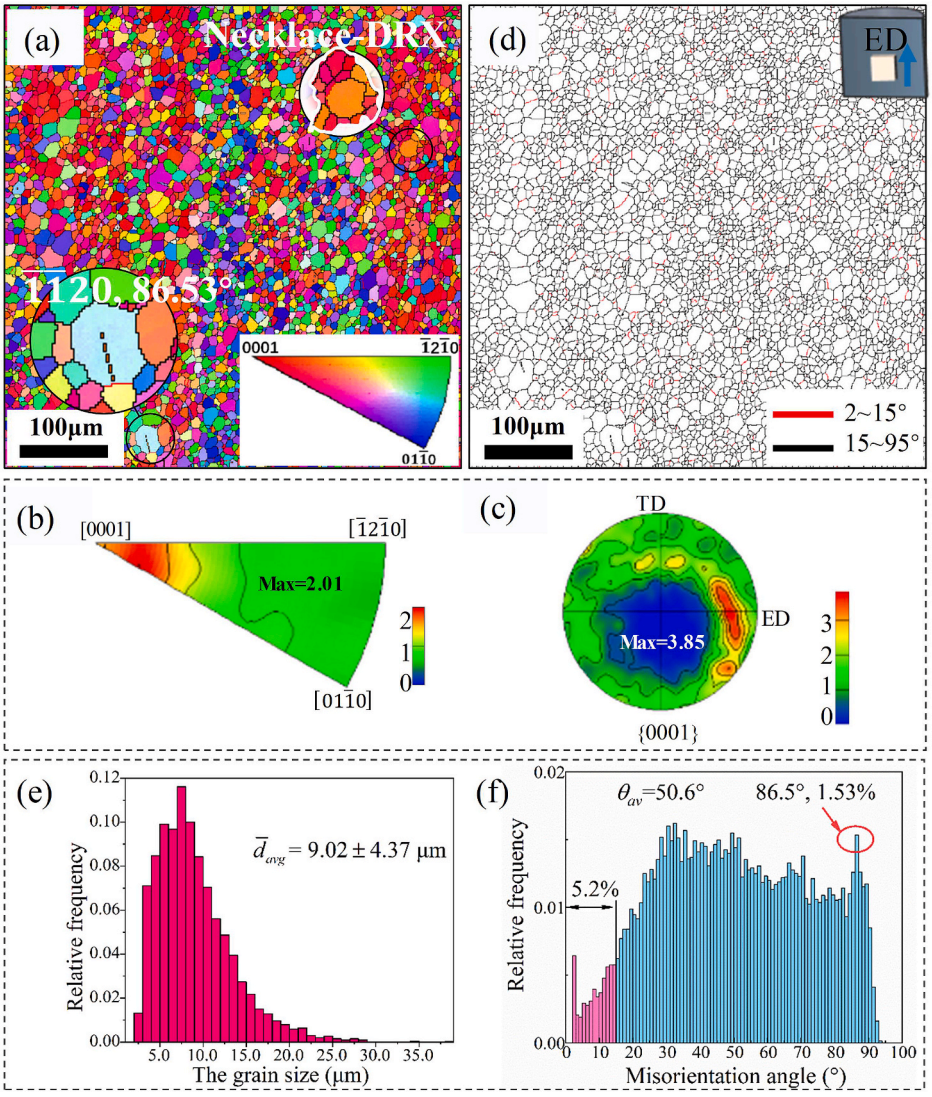

Fig. 4. The microstructure of as-received Zn-0.033 Mg alloy: (a) Inverse pole figure map, (b,c) corresponding inverse pole figure of ED plane and {0001} pole figure map, (d) grain boundary map, (e) grain size distribution, (f) distribution frequency histogram of misorientations.

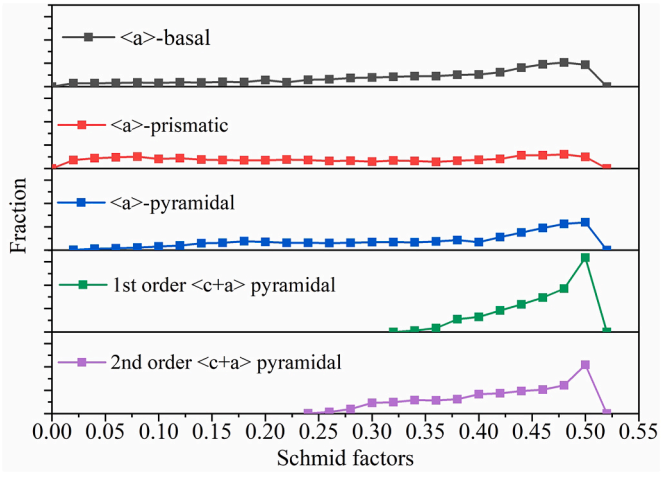

Fig. 5. Schmid factor distributions of various main slip systems of the as-received sample.

replaced the original coarse grains, and the grain size range was reduced within a range of 0.2–5 μm. With more ECAP passes, the grains of 12p-ECAPed sample represented a characteristic of bimodal grain size distribution characteristic, with a high frequency of less than 0.5 μm, and secondarily in the range of 1–1.5 μm. The fraction of ultrafine grains (less than 1.0 μm) in the 12p-ECAPed sample was 37.4%, which was much higher compared to 4p- and 8p-ECAPed samples with a fraction of 28.1% and 24.3%. This implied that the grains were significantly refined with the accumulating strain in the ECAP process. The formation of ultrafine grains appeared to be strongly correlated with further refinement of 12p-ECAPed sample, where new grains were generated at the boundaries of the primary large grains. This bimodal refinement microstructure, accompanied by substantial equiaxed grains, was attributed to DRX during ECAP, which was typically responsible for the refinement of HCP metals with high stacking fault energies, occurring during severe plastic deformation [27]. Moreover, the average grain size of the 8p-ECAPed sample increased slightly from 1.53 ± 0.81 μm to 1.71 ± 0.94 μm, compared to the 4p-ECAPed sample, which was attributed to the expansion of DRX [28]. Fig. 6a revealed a necklace-shaped structure of grains, and the orientation of the fine-grained chains with similar orientations to the central grains. This microstructural characteristic was typically produced by discontinuous DRX [29]. Thus, new recrystallized grains were formed at the boundaries of the parent grains, and

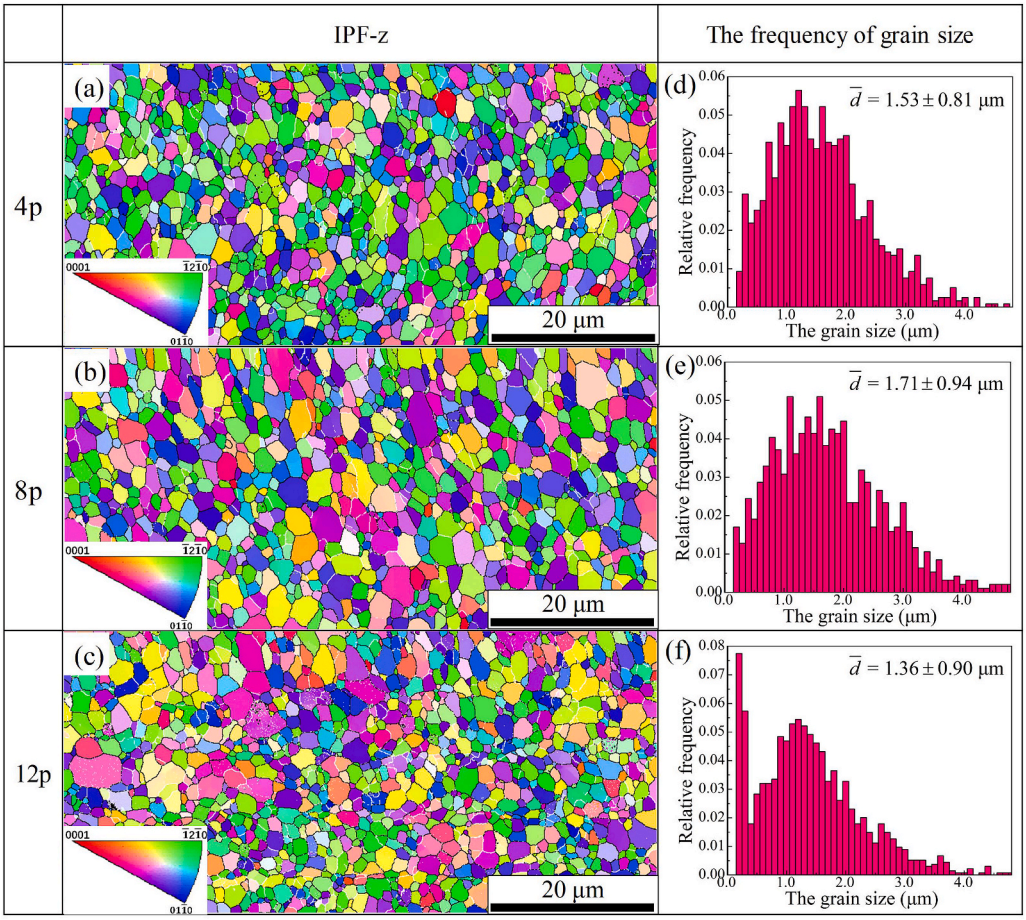

Fig. 6. EBSD observation results of 4p-, 8p- and 12p-ECAPed samples: (a,b,c) the inverse pole figure maps and (d,e,f) corresponding grain size distributions.

developed from the newly generated sub-boundaries, which were generally small in size and formed DRXed-grain chains, i.e., the "necklace" structure of DRXed-grain chains [28]. Moreover, the new DRXed-grain chains were formed by the bulging of the prior grain boundaries, and their orientations were close to the orientations of the parent grains. The existence of this type of structure confirmed that DRX was the major grain refinement mechanism for the ECAPed Zn-0.033 Mg alloy. As deformation progressed and the grains became refined, it was difficult to continue to generate DRXed grains through the expansion of the "necklace" structure, i. e, the expansion of DRX, due to the formation of the necklace structures by boundaries bulging to spread out at the DRXed-grain front [28]. Fig. 6b shows that the major color code of the grains after 8 ECAP passes was obviously different from that of the 4 ECAP passes (in Fig. 6a), and the orientation correlation between DRXed grains and the adjacent parent grains disappeared mirrored that the DRXed grains underwent continuous reorientation in the ECAP process. This indicated that the expansion was proceeded through other mechanisms other than boundaries bulging. Previous studies [30] have confirmed that continuous DRX exhibited progressive lattice rotation crystallization, especially through subgrain-rotation nucleation. There also appeared to be evidence of continuous DRX activation in this study. This type of DRX process did not develop subgrain structures but eventually developed subgrains along the existing grain boundaries. Furthermore, the misorientation of subgrains gradually accumulated until a regular grain character was obtained. Therefore, the transformation of the recrystallization caused slight coarsen in the grain size, and the progressive subgrain rotation recrystallization was an important refinement mechanism during the ECAP process [30].

To further explore the mechanism of grain refinement during ECAP, the evolution of the misorientation of adjacent grain boundaries was investigated. Fig. 7 displays the grain boundary profiles and the histogram maps of relative frequency of the misorientation angles for the ECAPed samples, where LABGs are distinguished with green lines. Fig. 7d–f shows the misorientation fraction of 4p-, 8p- and 12p-ECAPed samples. LAGBs fractions of ECAPed samples were all considerably higher than that of as-received sample, especially when the misorientation angle was less than 5° with a large peak. The LAGB fractions of 4p-, 8p- and 12p-ECAPed samples were 34.7%, 28.3% and 44.4%, respectively, and the average misorientation angles were calculated as 38.5°, 41.1° and 31.0°, respectively. For the 4p-ECAPed sample, the fraction of multiplied LAGBs increased to 34.7% compared to the as-received state of 5.2% and the small misorientation boundaries were widely scattered around relatively large grains, and even served as partial boundaries of some large grains. After further passes, the small misorientation boundaries of 8p-ECAPed sample were conspicuously diminished and became uniformly distributed, and the peak fraction of the misorientation angle less than 5° substantially declined, which was attributed to the continuous DRX of the progressive lattice rotation nucleation. Moreover, the LAGBs fraction of 12p-ECAPed sample notably increased to 44.4% and the LAGBs assembled in the subgrain region, indicating that ECAP created substantial subgrain structures, although recrystallization behavior did occur. Thus, the substructure correlated quite well with the grain refinement process, due to sub-boundary accommodation with the accumulating strain. The sub-boundary structure would contribute to subdividing primary large grains by LAGBs [31]. In Fig. 7d, a second peak fraction at a misorientation of 88.5° was observed, and its fraction reached 4.3%, which was attributed to the twin boundaries caused by excessive strain accumulation after 4 ECAP passes. This indicated that twinning was slightly stimulated, which coordinated deformation due to huge amount of shear strain, compared to the

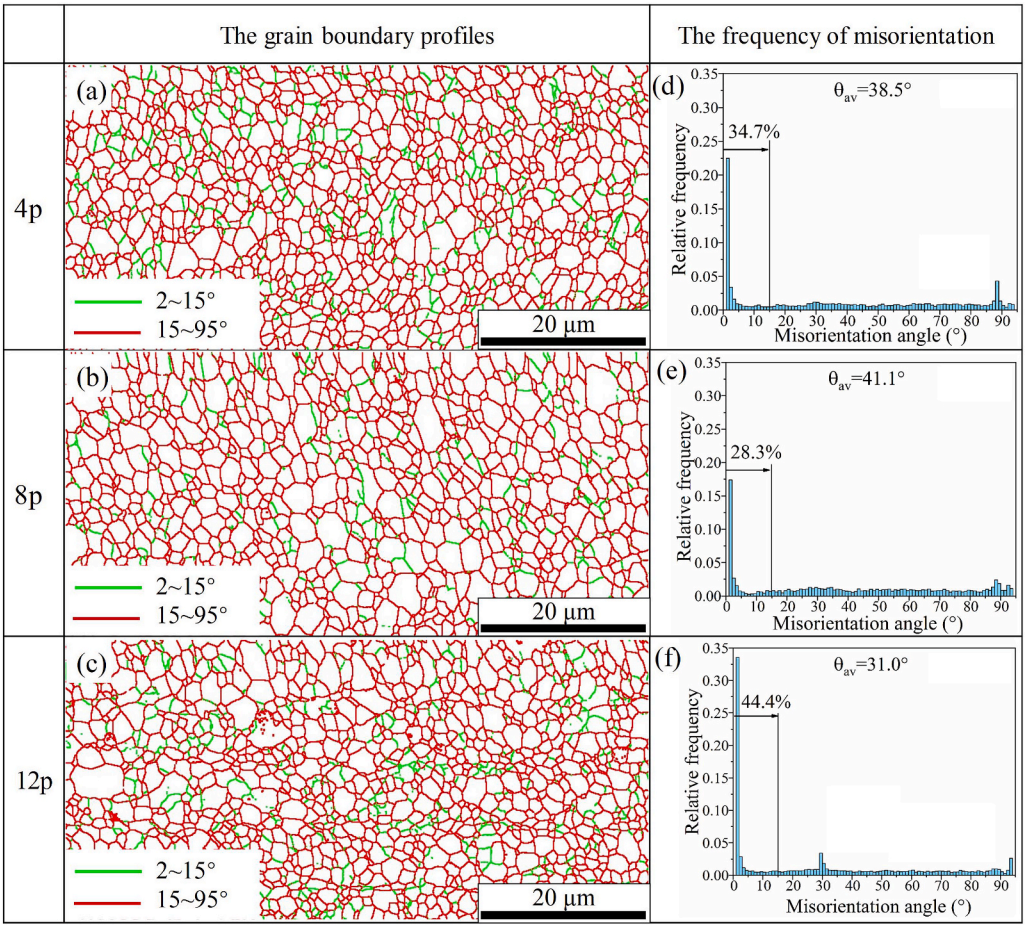

Fig. 7. Microstructural evolution of Zn-0.033 Mg with various passes: (a,d) 4p-ECAPed samples, (b,e) 8p-ECAPed samples, and (c,f) 12p-ECAPed samples (In the boundary maps, HAGBs (>15°) in red lines ; LAGBs (≤15°) in green lines). (For interpretation of the references to color in this figure legend, the reader is referred to the Web version of this article.)

as-received sample. However, deformation was still dominated by dislocations. Reports have shown that the deformation mechanism of as-drawn Zn-0.02 Mg gradually transitioned from twins to dislocations during deformation [16]. In addition, the refinement could suppress twinning to a certain extent [32]. The boundaries vanished after 8 ECAP passes process due to the sufficient recrystallization and the assistant nucleation mechanism of progressive subgrain rotation recrystallization [33,34]. After 12 ECAP passes, the LAGBs fraction increased again, and a fairly large number of misorientation angle at 2°, with the peak fraction of 33.55%, was observed. In addition, second peak fractions of 30° and 94° were noticed (Fig. 7f), which were accompanied by the formation of numerous substructures (Fig. 7c). This type of grain boundary occurred as a result of preferential nucleation due to the Mg_2Zn_{11} particle stimulated nucleation (PSN) mechanism, and growth of DRXed grains due to high mobility compared with other grain boundaries [35]. The second-peak orientation angle of the DRXed grains might be induced by excess strain accumulation, which was accompanied by the formation of a large number of substructures [36]. This mirrored the nucleation mechanism of discontinuous DRX in this stage.

To reveal the effects of ECAP on the DRX process, the grain orientation spread (GOS) value was calculated, which was the average difference in orientation between the average grain orientation and all measured points in one grain [37]. The GOS method can evaluate the volume fraction of DRX grains to a certain extent, based on the principle that the GOS value of DRXed grains will be lower than that of deformed grains [38]. The GOS threshold can be determined by the endpoint of the first prominent peak in the GOS distribution curve, and defined by the differences between recrystallized grains and deformed grains [37]. The GOS value distributions of the as-received, 4p-, 8p- and 12p-ECAPed samples are shown in Fig. 8; according to the statistical results, the GOS thresholds of as-received, 4p-, 8p- and 12p-ECAPed samples were determined as 1°, 0.9°, 1.4°, and 1°, respectively. Since recrystallization can effectively absorb deformation energy and dislocations, a smaller average GOS value was generally associated with a less geometrically necessary dislocation to a certain extent. A higher average GOS value indicated that the geometrically necessary dislocations were more likely larger, and the samples had accumulated greater strain energies [39]. As shown in Fig. 8e, the average GOS values of the as-received and 4p-, 8p- and 12p-ECAPed samples were 0.89°, 0.67°, 0.58° and 0.73°, respectively. These results demonstrated that with increasing passes, dislocation accumulation gradually declined and the degree of recrystallization increased until 8 ECAP passes. After the 8th ECAP pass, the dislocation began to store up positively and the recrystallization weakened simultaneously with more passes. Before 8th ECAP pass, the GOS peak got shifted to the smaller GOS value signifying that a large number of grains had recrystallized. After 8 ECAP passes, the GOS peak of 12p-ECAP sample got moved to a larger value, implying that the DRX did not consume enough dislocations generated by ECAP.

The recrystallization maps can be used as a reference to distinguish the evolution of newly recrystallized grains and substructures and deformed grains, which are shown in Fig. 9a, based on the previously mentioned GOS approach [40]. The blue area denoted fully recrystallized grains, which contributed to stabilizing plastic deformation and preventing cracking during the ECAP process. The yellow and red area, i.e., non-recrystallized region, obviously declined in size as the ECAP passes increased, indicating that more complete recrystallization.

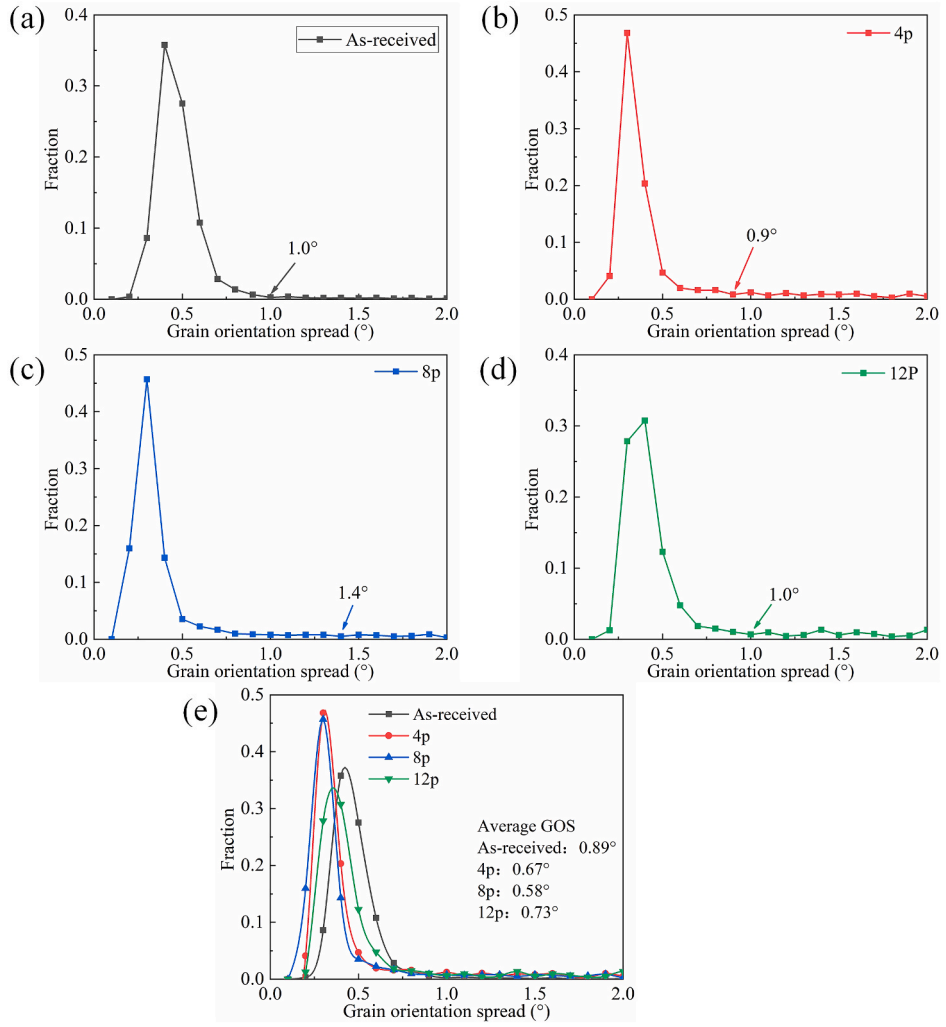

Fig. 8. The grain orientation spread distributions of Zn-0.033 Mg: (a) as-received sample, (b) 4p-ECAPed sample, (c) 8p-ECAPed sample, (d) 12p-ECAPed sample, (e) the combination map of four curves from Fig. 8a–d.

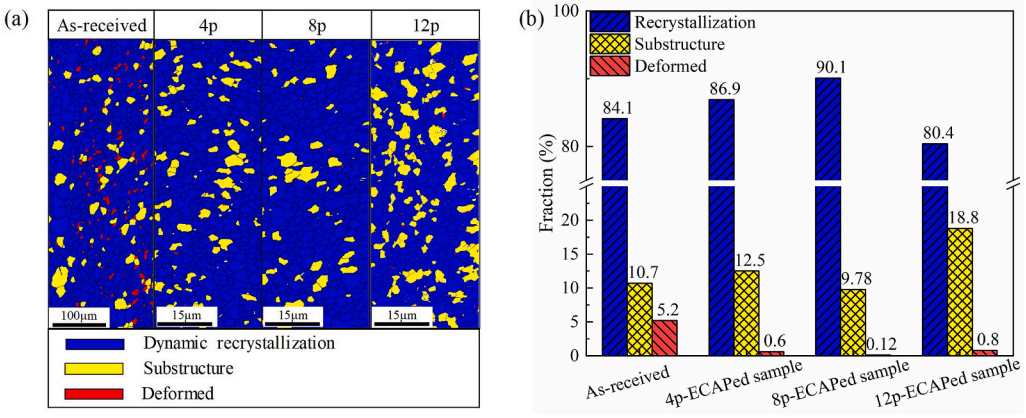

Fig. 9. The distribution maps of recrystallized grains: (a) The character distribution maps of recrystallized grains (blue stands for fully recrystallized grains, yellow for substructure and red for deformed), and (b) the fraction of grains that underwent recrystallization. (For interpretation of the references to color in this figure legend, the reader is referred to the Web version of this article.)

Fig. 9b shows a statistical percentage of DRXed grains. The DRXed-grain percentages of as-received, 4p-, 8p- and 12p-ECAPed samples were 84.1%, 86.9%, 90.1% and 80.4%, respectively. These fractions were consistent with the above analysis results, indicating that until 8 ECAP passes had completed recrystallization. Afterward, an increasing ECAP passes restricted the recrystallization process. Moreover, the fractions of the substructure and the deformed grains both increased significantly for the 12p-ECAPed sample, indicating excessive accumulation of strain energy and high dislocation density.

The kernel average misorientation (KAM) value is defined as the

average value of the difference in orientation between each pixel and its neighboring pixels. It represents the average misorientations between the points in the local area and the center, and can reflect the arrangement and accumulation of dislocations to a certain extent [41,42]. To further illustrate the effect of ECAP on microstructural evolution, the KAM maps of as-received and ECAPed samples are shown in Fig. 10, which were retrieved from the misorientation of EBSD data. Fig. 10a shows that the KAM value of as-received sample was very high, revealing that a high accumulation of dislocations in the material after two-step swaging. Low KAM values of ECAPed samples were mainly concentrated inside the grains, while high KAM values were mainly located in the boundaries around the grains. Thus, dislocation evolution played a vital role in the nucleation and growth of DRXed grains through stimulating nucleation, consuming dislocations, and alleviating deformation. In the early stage of ECAP, accompanied by significant grain refinement, the KAM value of 4p-ECAPed sample was greatly reduced, compared to the as-received sample indicating that the dislocations consumed by DRX exceeded the accumulation of dislocations caused by plastic deformation in this ECAP stage. As the ECAP passes increased, the KAM values of the 8p-ECAPed sample further decreased, while the fraction of HAGBs increased via the translation from LAGBs. In addition, the grain size grew slightly, due to the synergistic consumption effect of continuous DRXed and dynamic recovery. After 12 ECAP passes, the KAM values increased significantly, and LAGBs and the substructures increased greatly, but the grain size reduced. These results manifested that recrystallization had occurred but was not sufficient to offset dislocation accumulation. In addition, the KAM map was also used to visualize the geometrically necessary dislocation density distributions [43]. The KAM map of 12p-ECAPed sample showed a remarkable increase in geometrically necessary dislocation density, which may be responsible for both increasing the LAGBs and further refinement. The sub-boundaries formed by these dislocations apparently stimulated the refinement of the original grains into subgrains [44].

Fig. 10b displays the relative frequency curve of KAM values in the samples before and after several ECAP passes. The KAM distribution can be considered as a regime with high and low dislocation densities [45]. It could be identified with two regions, i.e., a lognormal KAM distribution in the range of above 0.05° and a small average value of KAM (dashed rectangle zone) implying randomly distributed small local strain. The as-received sample exhibited a high relative frequency of large KAM values (more than 0.5°), while the ECAPed samples all existed a high relative frequency of the small KAM values (lower than 0.5°). This suggested that the free-strain region increased, and dislocation accumulation was restricted via ECAP. This was considered as proof of the occurrence of DRX during ECAP, with increasing fraction of recrystallization and grain size refinement. Moreover, for the 8p-ECAPed sample, 90.1% of recrystallization and 71.1% of HAGBs were considered evidence of continuous DRX in this stage. Until 12 ECAP passes, the fraction of the small KAM region reduced, while the normal distribution crest moved to the right, which confirmed that the dislocations changed high-density dislocations with a homogeneous arrangement.

For HCP metals, texture plays a critical role in the mechanical properties of ECAPed zinc alloy, as important as grain size. Texture changes were presented by the IFPs, with correlated pole figures due to the asymmetry of the HCP crystal structure. The IPF maps of ED plane and {0001} pole figure maps are demonstrated in Fig. 11. With the increasing ECAP passes, the texture intensity of ECAPed samples increased (Fig. 11e,f,g). However, the orientation axis of ECAPed samples on the ED plane tilted slightly during ECAP processing, compared to a typical <0001> fiber texture in the as-received state, which was aligned with ED (Fig. 4b). Texture evolution of other Zn–Mg alloy also has been reported, such as Zn-1.6 Mg, which was subjected to a rotary die-ECAP process [46], and Zn-0.02 Mg, which was subjected to a rolling process [16]. Thus, shifts of texture have been previously reported, and worthy of further study. It seemed that this transformation exhibited a strong correlation with the DRX development during plastic deformation. EBSD IPF analysis of ECAPed samples showed that the relatively strong texture was formed deviating away from <0001> axis 50 °–70° (in Fig. 11a–c). For the 4p-ECAPed sample, a second texture component was generated on the ED plane, in the form of a weak component between [0001] and $[\bar{1}2\bar{1}0]$, tilting about 60° away from <0001>. This indicated that the reorientation of newly generated DRXed grains had occurred. However, dislocations that resulted from ECAP driven rotation process would be stored at boundaries, and thus induced internal stress would form within the material [47]. Once the internal stress was high enough to activate the cooperative dislocation rearrangement, it would generate new strain-induced boundaries. For the 12p-ECAPed sample, the pole intensity in {0001} pole axis was 13.04, which was attributed to the newly generated DRXed grains due to the repeated iterations of recrystallization and dynamic recovery processes during ECAP.

3.2. Effect of ECAP on mechanical properties

To study the effect of ECAP on the deformation behavior of ultrafine-grained Zn-0.033 Mg alloy, and establish a the relationship between microstructure and mechanical properties, the uniaxial tensile tests were performed at room temperature. Fig. 12 depicts the engineering stress-strain curves of the samples with various ECAP passes. The results showed that the as-received sample exhibited continuous yielding behavior, while the ECAPed samples presented a discontinuous yielding phenomenon. In addition, the yield strength was significantly improved by ECAP process.

The as-received sample showed significant work hardening after the onset of yielding, and deformed uniformly. The yield stress and elongation were 166 ± 7 MPa and 40.09 ± 4.37%, respectively. These values were much higher than the as-extruded Zn-0.02 Mg alloy reported by

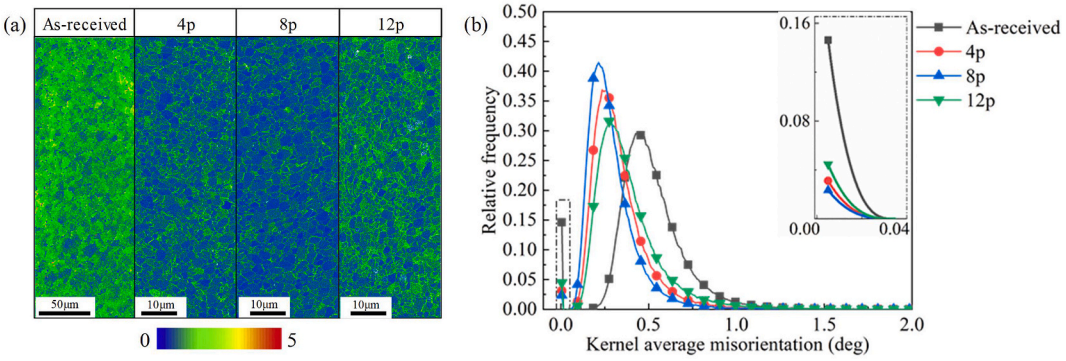

Fig. 10. Distribution of kernel average misorientation (KAM) values: (a) KAM maps of as-received, 4p-, 8p- and 12p-ECAPed samples; (b) the corresponding relative frequency of KAM values.

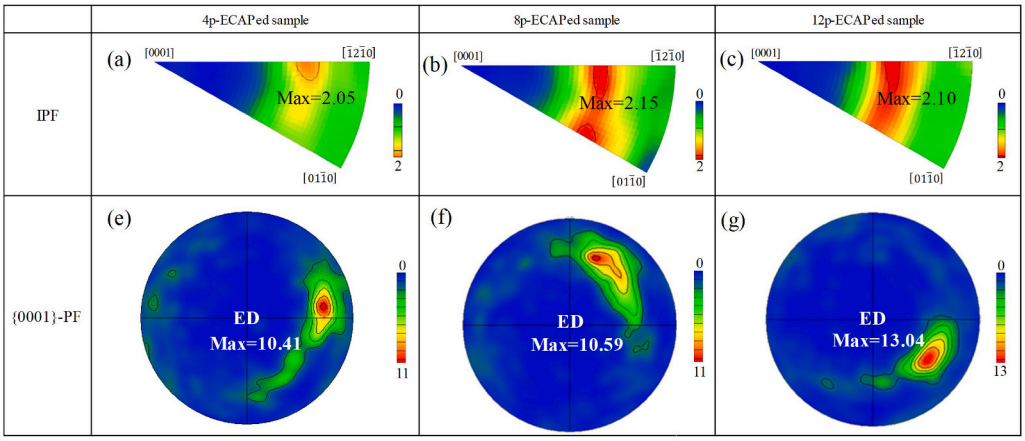

Fig. 11. Texture evolution of Zn-0.033 Mg alloys during ECAP process: (a,e) 4p-ECAPed sample, (b,f) 8p-ECAPed sample and (c,g) 12p-ECAPed sample.

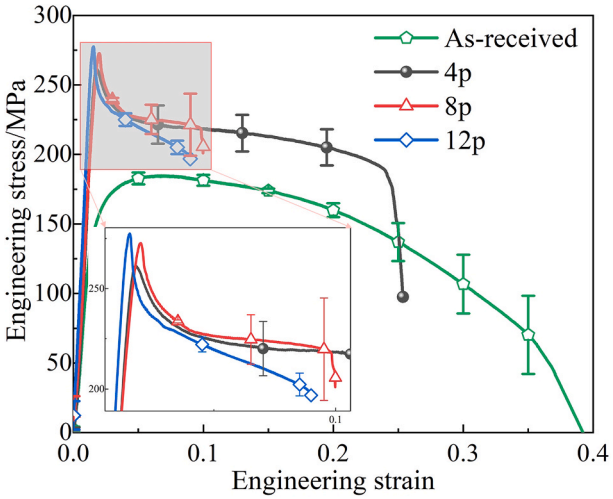

Fig. 12. Engineering stress-strain curves and the magnified plot of the yield drop region.

Ref. [16] which had a grain size of 25 μm. According to the Zn–Mg binary alloy phase diagram, Zn–Mg alloy in this study was composed of α-Zn matrix and Mg_2Zn_{11} intermetallic compounds, which have also been observed in zinc alloys with similar magnesium content [48]. Furthermore, Mg_2Zn_{11} content increased with the alloying magnesium content. Shen et al. [49] pointed out that after hot extrusion, the grains became refined and homogeneous, and the area fraction of the eutectic region was reduced. Liu et al. [50] also proposed that after multi-pass ECAP, the eutectic structure was crushed into fine particles and mixed with DRXed grains. Thus, second phase strengthening should exist to better investigate Zn-0.033 Mg alloy. However, compared to the contributions of grain boundary refinement toward strength, the effect of this factor was weak due to the lower magnesium content in this alloy. The ECAPed samples reached the peak stress rapidly, which was the upper yield point. The flow stress dropped to the lower yield point, and subsequently entered into a steady-state until fracture for the 4p-ECAPed sample. In contrast, in the 8p- and 12p-ECAPed samples, the stress continued decreasing after yielding, and eventually fractured. In this situation, except for the section near the fracture point, the rests of the uniaxial tensile specimens were virtually undeformed [51], and the lower yield point was higher than the ultimate tensile stress at the fracture point, as shown in Fig. 12. In the inset of Fig. 12, the strain-softening of 8p-ECAPed sample was relatively weaker compared to other ECAPed ones. It was speculated that this was attributed to the complete DRX grains of 8p-ECAPed sample, and slightly large grain generated.

The deformation process of 4p-ECAPed sample is depicted in Fig. 13, which consisted of a stress drop accompanied by yielding and a steady-state until fracture. A yield stress drop typically occurred in ultrafine-grained materials, and was called the yield point phenomenon [52]. Thus, combined with the macroscopic characteristics of the specimen gauge length during the uniaxial tensile testing, it could be inferred that result corresponded to Lüders bands. Therefore, the deformation process was comprised of the initiation of Lüders bands, nucleation, and then propagation until fracture, as shown in the insets of Fig. 13. Lüders deformation was observed when discontinuous yielding occurred in the fine-grained samples during plastic deformation, which was also consistent with the results of ECAPed samples in this study. Currently, there are two popular explanations for the yield point phenomenon in literature. One explanation proposed by Cottrell and Bilby [53] suggested that the dislocations become locked by a Cottrell atmosphere. Another explanation suggests an insufficient initial mobile dislocation density leads to the abrupt yield stress drop [54]. According to the former theory, the addition element Mg segregates to the dislocation strain fields, and high stress is needed to overcome the obstacles of Mg solute atoms. Consequently, under the actions of external force, high stress was required to overcome the Mg atoms. As the dislocations hurdle the restrictions in the form of barrier Mg, the stress required to move dislocations was much smaller, resulting in the yield drop [55].

For a given strain rate, the velocity of dislocation movement is inversely proportional to the density of mobile dislocations based on the Taylor equation, which is expressed as a function of dislocation density and dislocation movement:

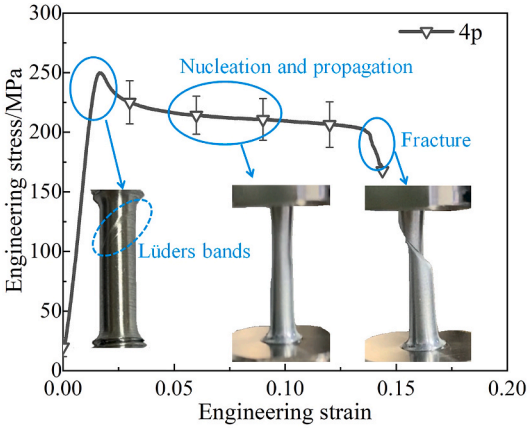

Fig. 13. The tensile deformation process of 4p-ECAPed sample at room temperature.

$$\dot{\varepsilon} = b\rho_m v \quad (2)$$

where b is the Burgers vector, ρ_m denotes the density of the mobile dislocations, and v is the velocity of dislocations. Thus, a large external stress was required to generate large dislocation velocities, and maintain the plastic strain rate when the materials exhibited a low initial mobile dislocation density. This was associated with the upper yield point for ECAPed samples entering the plastic state rapidly through the elastic regime. As deformation continued, the dislocation velocity decreased due to increasing mobile dislocation density caused by multiplication, and this was attributed to the yield drop of ECAPed samples.

Fig. 14 presents the yield strength and elongation of samples, as a function of the number of ECAP passes and corresponding grain size, where $\triangle\sigma$ denotes the yield drop value, which was defined as the difference between the upper and lower yield stresses. Both the upper yield stress and $\triangle\sigma$ increased with the ECAP passes increased. Furthermore, the $\triangle\sigma$ value was related to the initial mobile dislocation density in the material. Thus, the effects of mobile dislocation density on yield behavior were well rationalized by Hahn's model [54]. The mobile dislocation density of ECAPed samples was very low, as the dislocations were locked by solute atoms blocked by stacking and grain boundaries. Thus, a larger external stress was required to move the mobile dislocations at a high velocity, to maintain the plastic deformation strain rate. A high yield stress was consequently generated, which became the upper yield stress. As plastic strain increased, an abrupt multiplication of dislocations caused a significant decrease in the externally loaded stress, which produced the yield drop phenomenon on the stress-strain curve. As shown in Fig. 14, the $\triangle\sigma$ of the 4p-ECAPed sample was 33 ± 3 MPa, while those of the 8p- and 12p-ECAPed ones were 53 ± 4 MPa and 60 ± 7 MPa, respectively. Thus, the more passes, the greater the yield drop, creating a more obvious yield point phenomenon. This demonstrated that as the passes increased, the mobile dislocation density decreased, despite the increasing amount of accumulated dislocations and plastic deformation strain (as shown in Fig. 10a). This results were consistent with the dislocation density simulation results, as a function of strain using the mobile/immobile dislocation models, as reported by Bratov et al. [56].

The commonly used pile-up model for explaining the Hall-Petch relationship (Eq. (3)), k_y is usually considered to sign the ability to resist the slip transmission of grain boundaries, such as from one grain to the neighbor, which also means the grain boundary strength.

$$\sigma_y = \sigma_0 + k_y d^{-\frac{1}{2}} \quad (3)$$

Many previous studies have reported that a correlation between the Hall-Petch slope and yield behavior, regardless of the conventional or ultrafine grain sizes. However, for the zinc alloy in this work, this correlation was not valid. Wang et al. [57] found that when the grain size was reduced to about 1 μm, the material exhibited a significant transition from continuous yield behavior to discontinuous yield behavior during the plastic deformation. A large volume fraction of grain boundaries, due to the presence of ultrafine grains, provided a high density of dislocation source, which resulted in a rapid increase in dislocation density.

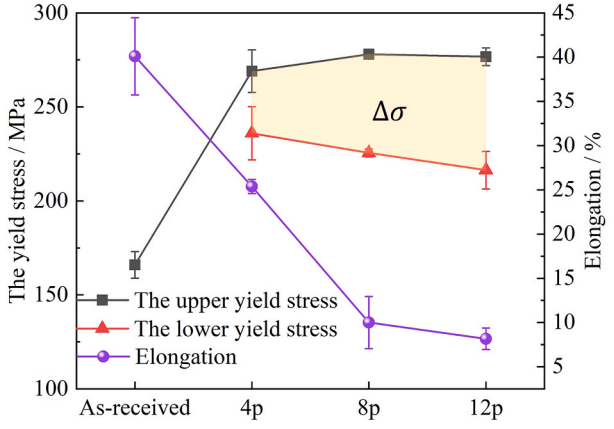

Fig. 14. The dependence of yield strength and elongation on the ECAP passes.

In addition, Petch also proposed another explanation for the grain size dependence of discontinuous yield in 1962, in the form of a micro-yielding model. Petch showed that plastic deformation was localized in these micro-yielded grains in the polycrystalline structure during discontinuous yielding. The local strain rate was much higher in the yielded grains, compared to the macroscopic strain rate exerted by the tensile test machine. Thus, in the engineering stress-strain curves of ECAPed samples, the lower yield stress was greater than the ultimate tensile strength, and fracture occurred at the point where the Lüders bands nucleated, while the rest of the sample was virtually unstrained. A similar conclusion was also achieved by Rooyen [51]. Because this type of plastic deformation only occurred in the local region of the gauge length, the yield strength was affected by the grain size and other microstructural characteristics, such as dislocation distribution and crystallographic orientation. As grain size decreased, the yield stress decreased, which was due to the increased contribution of grain boundary slip toward total deformation [58]. After 12 ECAP passes, the elongation decreased to 8.17 ± 1.21%, which resulted from deformation instability during the early stages of deformation. In ultrafine-grained materials, smaller grains typically inhibited the generation and storage of dislocation necessary for strain hardening [59]. Thus, the work hardening rate must be increased to delay necking and improve the strain to failure for UFG-ECAPed samples. For other ECAPed alloys, it has been reported that low-temperature or short-duration annealing achieved improvements in both ductility and high strength [60,61]. Thus, an effective and appropriate thermal treatment for 12p-ECAPed sample, to recover ductility, would be investigated further.

The above texture analysis revealed that ECAP process achieved significant microstructure refinement and homogenization, but introduced different strong texture components. For HCP metals, the evolution of texture can govern the Schmid factors of different slip systems and effect various mechanical properties, especially ductility. This can be related to the c/a ratio of the alloy, which had an ideal value of nearly 1.633, and tended to form a basic fiber texture with a higher Schmid factor, resulting in lower yield stress and excellent elongation. Thus, in zinc (c/a = 1.856, which exceeds the ideal value), there is a lower critical resolved shear stress (CRSS) of pyramidal $\{11\bar{2}2\}\langle 11\bar{2}3\rangle$ than prismatic $\{10\bar{1}0\}\langle 11\bar{2}0\rangle$ slip system [18]. Thus, a combination of basal slip and pyramidal slip systems drove the texture evolution, where the basal pole tilted toward away to ED during ECAP process. This deformation mode was supported by taking into account the texture distribution and slightly increased texture intensity of the sample (Fig. 11). The results confirmed that the newly generated DRXed grains had slightly rotated, and most of the grains exhibited textures with basal poles tilted away from the ED, which was consistent with previous reports in the literature [6].

Fig. 15 plots the Schmid factors for main slip systems. It was obvious that ECAPed samples had lower Schmid factors for the basal slip system, suggesting that most grains on the basal plane were in hard orientations related to the tensile direction. Thus, the deformation mechanism of non-basal <c+a> slip system was activated, and sustained plastic deformation, such as the pyramidal <c+a>-type slip system [62]. Comparing the IPF of ED plane between the 4p- and 8p-ECAPed samples (in Fig. 11a and b), it was confirmed that the DRXed fined grains in the 4p-ECAPed sample provided greater actuation of pyramidal slip. This was consistent with the high average Schmid factor values of <a> pyramidal slip in the 4p-ECAPed sample (Fig. 15). Thus, the 4p-ECAPed sample exhibited a larger elongation, due to the coordinated deformation of the non-base slip system. In addition, because the pyramidal

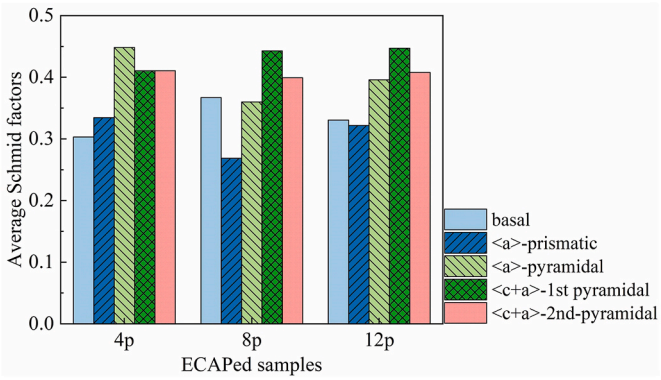

Fig. 15. The average Schmid factors for diverse slip systems of ECAPed samples.

CRSS for <c+a> slip system was higher than that for <a> slip, a larger stress was required to actuate it, which resulted in the higher yield strength in the 8p- and 12p-ECAPed samples, compared to that in the 4p-ECAPed sample. The non-basal slip could control the macroscopic response and internal strain development in the sample [63], even though the basal slip accommodated the majority of the strain during tensile deformation. These results thus suggested that the most active non-basal slip system in Zn-0.033 Mg during the warm-ECAP process was the <c+a>-pyramidal slip system. Consequently, an important factor of yield strengthening was ascribed to the ultrafine-grained boundaries, dislocation, and texture strengthening caused by ECAP.

3.3. Effect of ECAP on corrosion behavior

As a possible material for degradable vascular stents, corrosion resistance is critical. Fig. 16a shows the corrosion rates of the samples after immersion testing in Hank's artificial body fluid for several days. The corrosion rates of the investigated samples rapidly abated in the first four days, then gradually decreased, and finally stabilized. The stable rate of about 0.02 mm/year was achieved for as-received samples, and 0.004–0.01 mm/year for ECAPed samples after immersion for 14 days. For the as-received sample, the corrosion rate was more than double the rate of ECAPed samples, suggesting that the ECAP process sufficiently improved the degradation performance of Zn-0.033 Mg. However, for the 12p-ECAPed sample, the rate was overall higher than the other two ECAPed samples, due to the increase in grain boundaries stemming from a substantial number of ultrafine grains. Moreover, the corrosion rate entered a steady state soon and was maintained at a rate of 0.01 mm/year, after immersion 4 days, as shown in Fig. 16a. This result was likely to be ascribed to the passive film composed of compact corrosion products covering the surface. With the increasing ECAP passes, the surface structure of ECAPed samples became more compact, and the micro-spatial structure between the grain boundaries was restrained. Thus, the distribution of corrosion products was more uniform, and would not be susceptible to surface deterioration.

Fig. 16b shows the corrosion rates of the Zn and Zn-0.05 Mg alloy, with grain sizes of approximately 100 μm and 10 μm [21], as well as the 12p-ECPAed sample in this study with a grain size of 1.36 ± 0.90 μm. Corrosion rate of the 12p-ECAPed sample obtained by the ECAP process exhibited an entirely opposite trend compared to Zn-0.05 Mg, in the first four days. Then the rates stabilized at approximately 0.15 mm/year and 0.01 mm/year, verifying the important effect of grain size on corrosion rate, especially at the ultrafine-grained level. This verified once again that the corrosion rate of the ultrafine-grained Zn–Mg alloy was significantly reduced by the ECAP process.

4. Conclusion

In the present study, an ultrafine-grained Zn-0.033 Mg (in wt.%) alloy was prepared by multi-pass equal-channel angular pressing (ECAP) at 416 K. The evolution of the microstructure, mechanical properties, and corrosion behavior of the material during the ECAP process was studied in detail. The main conclusions are drawn as follows.

(1) The warm ECAP process of the copper-clad sample is an effective way to fabricate the ultrafine-grained Zn-0.033 Mg. Substantial grain refinement is achieved through 12 ECAP passes, yielding an average grain size of 1.36 ± 0.90 μm.
(2) The average grain size is reduced from 9.02 ± 4.37 μm (in the as-received material) to 1.53 ± 0.81 μm after 4 ECAP passes and then slightly increased to 1.71 ± 0.94 μm after 8 passes owing to the continuous dynamic recrystallization of the progressive subgrain rotation nucleation. Simultaneously, a texture with extrusion direction deviating 70 ± 5° away from <0001> is formed by newly recrystallized grains during ECAP.
(3) A large number of low-angle grain boundaries and substructures are formed, and both the grain orientation spread and the kernel average misorientation are increased after 12 ECAP passes. Although further grain refinement is achieved with more ECAP passes, more dislocations accumulate, which is detrimental to ductility.
(4) The yield strength is ultimately enhanced to 276 ± 5 MPa after 12 ECAP passes, which can be put down to the synergy effect of grain refinement and texture and dislocation strengthening. An optimal properties combination of yield strength (263 ± 11 MPa) and elongation (25.37 ± 0.79%) at room temperature is obtained by 4 ECAP passes.

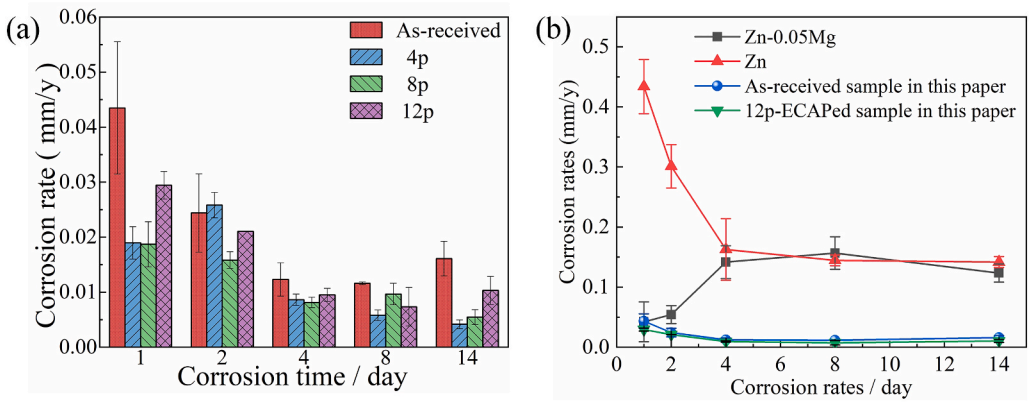

Fig. 16. Corrosion rates of the immersion tests for 14 days: (a) for Zn-0.033 Mg in Hank's and (b) for Zn and Zn-0.05 Mg in simulated body fluid [21].

(5) The ultrafine-grained Zn-0.033 Mg alloy exhibits uniform corrosion with a low corrosion rate of 0.004–0.01 mm/year, which fully fulfills the requirements for biodegradable implant material.

CRediT authorship contribution statement

Xiuping Wang: Conceptualization, Methodology, Validation, Investigation, Data curation, Writing – original draft, Writing – review & editing, Visualization. **Yan Ma:** Investigation, Validation, Writing – review & editing. **Bao Meng:** Conceptualization, Methodology, Formal analysis, Data curation, Resources, Writing – review & editing, Supervision, Funding acquisition. **Min Wan:** Resources, Supervision, Funding acquisition.

Declaration of competing interest

The authors declare that they have no known competing financial interests or personal relationships that could have appeared to influence the work reported in this paper.

Acknowledgments

The authors deeply acknowledge the support from the National Natural Science Foundation of China (Grant Nos.: 51975031 and 52075023) and Beijing Natural Science Foundation (No. 3172022).

References

[1] Y. Okamura, N. Hinata, T. Hoshiba, T. Nakatsuji, N. Ikeo, J. Furukawa, K. Harada, Y. Nakano, T. Fukumoto, T. Mukai, M. Fujisawa, Development of bioabsorbable zinc-magnesium alloy wire and validation of its application to urinary tract surgeries, World J. Urol. 39 (1) (2021) 201–208.
[2] Y. Liu, B.H. Lu, Z.X. Cai, Recent progress on Mg- and Zn-Based alloys for biodegradable vascular stent applications, J. Nanomater. 2019 (2019) 16.
[3] P.K. Bowen, A. Drelich, J. Drelich, J. Goldman, Rates of in vivo (arterial) and in vitro biocorrosion for pure magnesium, J. Biomed. Mater. Res. 103 (1) (2015) 341–349.
[4] P.K. Bowen, J. Drelich, J. Goldman, Zinc exhibits ideal physiological corrosion behavior for bioabsorbable stents, Adv. Mater. 25 (18) (2013) 2577–2582.
[5] H. Yang, C. Wang, C. Liu, H. Chen, Y. Wu, J. Han, Z. Jia, W. Lin, D. Zhang, W. Li, W. Yuan, H. Guo, H. Li, G. Yang, D. Kong, D. Zhu, K. Takashima, L. Ruan, J. Nie, X. Li, Y. Zheng, Evolution of the degradation mechanism of pure zinc stent in the one-year study of rabbit abdominal aorta model, Biomaterials 145 (2017) 92–105.
[6] E. Mostaed, M. Sikora-Jasinska, A. Mostaed, S. Loffredo, A.G. Demir, B. Previtali, D. Mantovani, R. Beanland, M. Vedani, Novel Zn-based alloys for biodegradable stent applications: design, development and in vitro degradation, J. Mech. Behav. Biomed. Mater. (2016) 581–602.
[7] L.B. Tong, J.H. Chu, W.T. Sun, Z.H. Jiang, D.N. Zou, K.S. Wang, S. Kamado, M. Y. Zheng, Development of high-performance Mg-Zn-Ca-Mn alloy via an extrusion process at relatively low temperature, J. Alloys Compd. 825 (2020) 10.
[8] V.E. Bazhenov, A.V. Li, A.A. Komissarov, A.V. Koltygin, S.A. Tavolzhanskii, V. A. Bautin, O.O. Voropaeva, A.M. Mukhametshina, A.A. Tokar, Microstructure and mechanical and corrosion properties of hot-extruded Mg–Zn–Ca–(Mn) biodegradable alloys, J. Magn. Alloys 2020 (2020) 15.
[9] J. Yan, Z. Qin, K. Yan, Mechanical properties and microstructure evolution of Mg-6 wt % Zn alloy during equal-channel angular pressing, Metals 8 (10) (2018) 11.
[10] Y. Ma, F.-Y. Han, C. Liu, M.-Z. Li, Microstructure, texture evolution, and mechanical properties of ECAP-processed ZAT522 magnesium alloy, Acta Metall. Sin. 33 (2) (2019) 233–242.
[11] C. Wang, A. Ma, J. Sun, H. Liu, H. Huang, Z. Yang, J. Jiang, Effect of ECAP process on as-cast and as-homogenized Mg-Al-Ca-Mn alloys with different Mg_2Ca morphologies, J. Alloys Compd. 793 (2019) 259–270.
[12] N. Skryabina, V. Aptukov, P. Romanov, D. Fruchart, P. de Rango, G. Girard, C. Grandini, H. Sandim, J. Huot, J. Lang, R. Cantelli, F. Leardini, Microstructure optimization of Mg-alloys by the ECAP process including numerical simulation, SPD treatments, characterization, and hydrogen sorption properties, Molecules 24 (1) (2019) 32.
[13] L.B. Tong, J.H. Chu, Z.H. Jiang, S. Kamado, M.Y. Zheng, Ultra-fine grained Mg-Zn-Ca-Mn alloy with simultaneously improved strength and ductility processed by equal channel angular pressing, J. Alloys Compd. 785 (2019) 410–421.
[14] M. Suresh, A. Sharma, A.M. More, R. Kalsar, A. Bisht, N. Nayan, S. Suwas, Effect of equal channel angular pressing (ECAP) on the evolution of texture, microstructure and mechanical properties in the Al-Cu-Li alloy AA2195, J. Alloys Compd. 785 (2019) 972–983.
[15] N. Martynenko, E. Lukyanova, V. Serebryany, D. Prosvirnin, V. Terentiev, G. Raab, S. Dobatkin, Y. Estrin, Effect of equal channel angular pressing on structure, texture, mechanical and in-service properties of a biodegradable magnesium alloy, Mater. Lett. 238 (2019) 218–221.
[16] L. Wang, Y. He, H. Zhao, H. Xie, S. Li, Y. Ren, G. Qin, Effect of cumulative strain on the microstructural and mechanical properties of Zn-0.02 wt%Mg alloy wires during room-temperature drawing process, J. Alloys Compd. 740 (2018) 949–957.
[17] W. Bednarczyk, M. Wątroba, J. Kawałko, P. Bała, Can zinc alloys be strengthened by grain refinement? A critical evaluation of the processing of low-alloyed binary zinc alloys using ECAP, Mater. Sci. Eng., A 748 (2019) 357–366.
[18] E. Mostaed, M. Sikora-Jasinska, J.W. Drelich, M. Vedani, Zinc-based alloys for degradable vascular stent applications, Acta Biomater. 71 (2018) 23.
[19] P.C. Gautam, S. Biswas, On the possibility to reduce ECAP deformation temperature in magnesium: deformation behaviour, dynamic recrystallization and mechanical properties, Mater. Sci. Eng., A 812 (2021) 141103.
[20] A. Jarzębska, M. Bieda, J. Kawałko, P. Koprowski, Ł. Rogal, R. Chulist, B. Kania, K. Sztwiertnia, W. Pachla, M. Kulczyk, Synergistic effect of Mg addition and hydrostatic extrusion on microstructure and texture of biodegradable low-alloyed zinc, IOP Conf. Ser. Mater. Sci. Eng. 375 (2018), 012008.
[21] C. Xiao, L. Wang, Y. Ren, S. Sun, E. Zhang, C. Yan, Q. Liu, X. Sun, F. Shou, J. Duan, H. Wang, G. Qin, Indirectly extruded biodegradable Zn-0.05wt%Mg alloy with improved strength and ductility: in vitro and in vivo studies, J. Mater. Sci. Technol. 34 (2018) 1618–1627.
[22] E. Hug, N. Bellido, Brittleness study of intermetallic (Cu, Al) layers in copper-clad aluminium thin wires, Mater. Sci. Eng., A 528 (22) (2011) 7103–7106.
[23] R. Lapovok, M. Dubrovsky, A. Kosinova, G. Raab, Effect of severe plastic deformation on the conductivity and strength of copper-clad aluminium conductors, Metals 9 (9) (2019).
[24] P.B. Prangnell, J.R. Bowen, P.J. Apps, Ultra-fine grain structures in aluminium alloys by severe deformation processing, Mater. Sci. Eng., A 375–377 (2004) 178–185.
[25] H. Jazaeri, F.J. Humphreys, The transition from discontinuous to continuous recrystallization in some aluminium alloys: I – the deformed state, Acta Mater. 52 (11) (2004) 3239–3250.
[26] L.B. Tong, M.Y. Zheng, S.W. Xu, X.S. Hu, K. Wu, S. Kamado, G.J. Wang, X.Y. Lv, Room-temperature compressive deformation behavior of Mg–Zn–Ca alloy processed by equal channel angular pressing, Mater. Sci. Eng., A 528 (2) (2010) 672–679.
[27] A. Jarzebska, M. Bieda, L. Maj, R. Chulist, D. Wojtas, M. Strag, B. Sulkowski, S. Przybysz, W. Pachla, K. Sztwiertnia, Controlled grain refinement of biodegradable Zn-Mg alloy: the effect of magnesium alloying and multi-pass hydrostatic extrusion preceded by hot extrusion, Metall. Mater. Trans., A-Phys. Metall. Mater. Sci. 51 (12) (2020) 6784–6796.
[28] D. Ponge, G. Gottstein, Necklace formation during dynamic recrystallization: mechanisms and impact on flow behavior, Acta Mater. 46 (1) (1998) 69–80.
[29] F.C. Liu, T.W. Nelson, Twining and dynamic recrystallization in austenitic Alloy 718 during friction welding, Mater. Char. 140 (2018) 39–44.
[30] B. Xie, B. Zhang, H. Yu, H. Yang, Q. Liu, Y. Ning, Microstructure evolution and underlying mechanisms during the hot deformation of 718Plus superalloy, Mater. Sci. Eng., A 784 (2020) 11.
[31] H. Masuda, E. Sato, Diffusional and dislocation accommodation mechanisms in superplastic materials, Acta Mater. 197 (2020) 235–252.
[32] N. Ecob, B. Ralph, The effect of grain size on deformation twinning in a textured zinc alloy, J. Mater. Sci. 18 (8) (1983) 2419–2429.
[33] J. Zhao, Y. Deng, J. Tang, J. Zhang, Influence of strain rate on hot deformation behavior and recrystallization behavior under isothermal compression of Al-Zn-Mg-Cu alloy, J. Alloys Compd. 809 (2019) 13.
[34] T. Sakai, A. Belyakov, R. Kaibyshev, H. Miura, J.J. Jonas, Dynamic and post-dynamic recrystallization under hot, cold and severe plastic deformation conditions, Prog. Mater. Sci. 60 (2014) 130–207.
[35] B. Li, M. Liao, Q. Ma, Z. McClelland, Structure of grain boundaries with 30 degrees 0001 misorientation in dynamically recrystallized magnesium alloys, Comput. Mater. Sci. 101 (2015) 175–180.
[36] A. Ostapovets, P. Šedá, A. Jäger, P. Lejček, Characteristics of coincident site lattice grain boundaries developed during equal channel angular pressing of magnesium single crystals, Scripta Mater. 64 (5) (2011) 470–473.
[37] Y. Cao, H.S. Di, J.Q. Zhang, J.C. Zhang, T.J. Ma, R.D.K. Misra, An electron backscattered diffraction study on the dynamic recrystallization behavior of a nickel-chromium alloy (800H) during hot deformation, Mater. Sci. Eng. 585 (2013) 71–85.
[38] W. Xu, X. Jin, D. Shan, B. Chai, Study on the effect of solution treatment on hot deformation behavior and workability of Mg-7Gd-5Y-0.6Zn-0.8Zr magnesium alloy, J. Alloys Compd. 720 (2017) 309–323.
[39] S. Dong, R. Chen, J. Guo, H. Ding, Y. Su, H. Fu, Deformation behavior and microstructural evolution of directionally solidified TiAlNb-based alloy during thermo-compression at 1373–1573K, Mater. Des. 84 (2015) 118–132.
[40] Y. Zong, D. Wen, Z. Liu, D.J.M. Shan, Design, γ-phase transformation, dynamic recrystallization and texture of a forged TiAl-based alloy based on plane strain compression at elevated temperature, Mater. Des. 91 (2016) 321–330.
[41] Z. Yang, A. Ma, H. Liu, J. Sun, D. Song, C. Wang, Y. Yuan, J. Jiang, Multimodal microstructure and mechanical properties of AZ91 Mg alloy prepared by equal channel angular pressing plus aging, Metals 8 (10) (2018) 14.
[42] A. Clair, M. Foucault, O. Calonne, Y. Lacroute, L. Markey, M. Salazar, V. Vignal, E. Finot, Strain mapping near a triple junction in strained Ni-based alloy using EBSD and biaxial nanogauges, Acta Mater. 59 (8) (2011) 3116–3123.
[43] H. Masuda, H. Tobe, E. Sato, Y. Sugino, S. Ukai, Transgranular dislocation activities and substructural evolutions accommodating two-dimensional grain boundary sliding in ODS ferritic steel, Acta Mater. 132 (2017) 245–254.

[44] H. Masuda, H. Tobe, E. Sato, Y. Sugino, S. Ukai, Two-dimensional grain boundary sliding and mantle dislocation accommodation in ODS ferritic steel, Acta Mater. 120 (2016) 205–215.
[45] Y. Zhong, F. Yin, T. Sakaguchi, K. Nagai, K. Yang, Dislocation structure evolution and characterization in the compression deformed Mn–Cu alloy, Acta Mater. 55 (8) (2007) 2747–2756.
[46] H. Huang, H. Liu, L.S. Wang, Y.H. Li, S.O. Agbedor, J. Bai, F. Xue, J.H. Jiang, A high-strength and biodegradable Zn-Mg alloy with refined ternary eutectic structure processed by ECAP, Acta Metall. Acta Metall. Sinica-English Lett. 33 (9) (2020) 1191–1200.
[47] Z. Zeng, M. Zhou, P. Lynch, F. Mompiou, Q. Gu, M. Esmaily, Y. Yan, Y. Qiu, S. Xu, H. Fujii, C. Davies, J.-F. Nie, N. Birbilis, Deformation modes during room temperature tension of fine-grained pure magnesium, Acta Mater. 206 (2021) 116648.
[48] H. Jin, S. Zhao, R. Guillory, P.K. Bowen, Z. Yin, A. Griebel, J. Schaffer, E.J. Earley, J. Goldman, J.W. Drelich, Novel high-strength, low-alloys Zn-Mg (<0.1wt% Mg) and their arterial biodegradation, Mater. Sci. Eng., C-Mater. Biol. Appl. 84 (2018) 67–79.
[49] C. Shen, X.W. Liu, B. Fan, P.H. Lan, F.Y. Zhou, X.K. Li, H.L. Wang, X. Xiao, L. Li, S. Zhao, Z. Guo, Z.J. Pu, Y.F. Zheng, Mechanical properties, in vitro degradation behavior, hemocompatibility and cytotoxicity evaluation of Zn-1.2Mg alloy for biodegradable implants, RSC Adv. 6 (89) (2016) 86410–86419.
[50] H. Liu, H. Huang, Y. Zhang, Y. Xu, C. Wang, J. Sun, J. Jiang, A. Ma, F. Xue, J. Bai, Evolution of Mg–Zn second phases during ECAP at different processing temperatures and its impact on mechanical properties of Zn-1.6Mg (wt.%) alloys, J. Alloys Compd. 811 (2019).
[51] G.T. Van Rooyen, Basic factors which influence the Lüders strain during discontinuous yielding, Mater. Sci. Eng. 7 (1) (1971) 37–48.
[52] S. Gao, M.C. Chen, M. Joshi, A. Shibata, N. Tsuji, Yielding behavior and its effect on uniform elongation in IF steel with various grain sizes, J. Mater. Sci. 49 (19) (2014) 6536–6542.
[53] A.H. Cottrell, B.A. Bilby, Dislocation theory of yielding and strain ageing of iron, Proc. Phys. Soc. 62 (1) (1949) 49–62.
[54] G.T. Hahn, A model for yielding with special reference to the yield-point phenomena of iron and related bcc metals, Acta Metall. 10 (8) (1962) 727–738.
[55] W.J. Kim, H.T. Jeong, Pronounced yield drop phenomenon at high temperatures in Al-Mg alloys with high contents of Mg (5–13 wt%), Mater. Sci. Eng., A 743 (2019) 590–596.
[56] V. Bratov, E.N. Borodin, Comparison of dislocation density based approaches for prediction of defect structure evolution in aluminium and copper processed by ECAP, Mater. Sci. Eng., A 631 (2015) 10–17.
[57] Y. Wang, Y. Tomota, T. Ohmura, W. Gong, S. Harjo, M. Tanaka, Continuous and discontinuous yielding behaviors in ferrite-cementite steels, Acta Mater. 196 (2020) 565–575.
[58] H.J. Choi, Y. Kim, J.H. Shin, D.H. Bae, Deformation behavior of magnesium in the grain size spectrum from nano-to micrometer, Mater. Sci. Eng., A 527 (6) (2010) 1565–1570.
[59] P.L. Sun, E.K. Cerreta, G.T. Gray, P. Rae, The influence of boundary structure on the mechanical properties of ultrafine grained AA1050, Mater. Sci. Eng., A 410–411 (2005) 265–268.
[60] Y. Gu, A. Ma, J. Jiang, H. Li, D. Song, H. Wu, Y. Yuan, Simultaneously improving mechanical properties and corrosion resistance of pure Ti by continuous ECAP plus short-duration annealing, Mater. Char. 138 (2018) 38–47.
[61] C.W. Su, L. Lu, M.O. Lai, Mechanical behaviour and texture of annealed AZ31 Mg alloy deformed by ECAP, Mater. Sci. Technol. 23 (3) (2007) 290–296.
[62] T. Liu, Y.D. Wang, S.D. Wu, R. Lin Peng, C.X. Huang, C.B. Jiang, S.X. Li, Textures and mechanical behavior of Mg–3.3%Li alloy after ECAP, Scripta Mater. 51 (11) (2004) 1057–1061.
[63] S.R. Agnew, D.W. Brown, C.N. Tome, Validating a polycrystal model for the elastoplastic response of magnesium alloy AZ31 using in situ neutron diffraction, Acta Mater. 54 (18) (2006) 4841–4852.